

<https://helda.helsinki.fi>

---

## Spatial Aggregation of Global Dry and Wet Patterns Based on the Standard Precipitation Index

Guan, Yanlong

2022-05

---

Guan , Y , Liu , J , Chen , A , Li , D , Jiang , Y , Cui , W , Lu , H , Pellikka , P , Heiskanen , J & Maeda , E 2022 , ' Spatial Aggregation of Global Dry and Wet Patterns Based on the Standard Precipitation Index ' , Earth's future , vol. 10 , no. 5 , e2022EF002720 . <https://doi.org/10.1029/2022EF002720>

---

<http://hdl.handle.net/10138/344318>

<https://doi.org/10.1029/2022EF002720>

---

cc\_by\_nc

publishedVersion

---

*Downloaded from Helda, University of Helsinki institutional repository.*

*This is an electronic reprint of the original article.*

*This reprint may differ from the original in pagination and typographic detail.*

*Please cite the original version.*




# Earth's Future



## RESEARCH ARTICLE

10.1029/2022EF002720

# Spatial Aggregation of Global Dry and Wet Patterns Based on the Standard Precipitation Index

Yanlong Guan<sup>1</sup> , Junguo Liu<sup>1</sup> , Aifang Chen<sup>1</sup>, Delong Li<sup>1</sup>, Yelin Jiang<sup>2</sup> ,  
Wenhui Cui<sup>1</sup>, Hongwei Lu<sup>3</sup>, Petri Pellikka<sup>4,5</sup>, Janne Heiskanen<sup>4,6</sup>, and Eduardo Maeda<sup>4,7</sup>

<sup>1</sup>School of Environmental Science and Engineering, Southern University of Science and Technology of China, Shenzhen, China, <sup>2</sup>Department of Civil and Environmental Engineering, University of Connecticut, Storrs, CT, USA, <sup>3</sup>Key Laboratory of Water Cycle and Related Land Surface Process, Institute of Geographic Science and Natural Resources Research, Chinese Academy of Science, Beijing, China, <sup>4</sup>Department of Geosciences and Geography, University of Helsinki, Helsinki, Finland, <sup>5</sup>State Key Laboratory for Information Engineering in Surveying, Mapping and Remote Sensing, Wuhan University, Wuhan, China, <sup>6</sup>Faculty of Science, Institute for Atmospheric and Earth System Research, University of Helsinki, Helsinki, Finland, <sup>7</sup>Area of Ecology and Biodiversity, School of Biological Sciences, Faculty of Science, University of Hong Kong, Hong Kong, China

### Key Points:

- A simplified patch-mosaic landscape framework was designed to characterize the spatial aggregation information of global drought patterns
- At the landscape level, the global aggregation degree increased since the 1980s
- At the class level, the correlation between total area and aggregation degree increased with an increase in dry/wet levels

### Supporting Information:

Supporting Information may be found in the online version of this article.

### Correspondence to:

J. Liu and H. Lu,  
[junguo.liu@gmail.com](mailto:junguo.liu@gmail.com);  
[luhw@igsnr.ac.cn](mailto:luhw@igsnr.ac.cn)

### Citation:

Guan, Y., Liu, J., Chen, A., Li, D., Jiang, Y., Cui, W., et al. (2022). Spatial aggregation of global dry and wet patterns based on the standard precipitation index. *Earth's Future*, 10, e2022EF002720. <https://doi.org/10.1029/2022EF002720>

Received 12 FEB 2022  
Accepted 9 MAY 2022

**Abstract** Quantifying the spatial integrity and patterns of dry/wet events over land is essential to understand how the local hydrological regime responds to environmental changes. Spatial aggregation changes in dry and wet areas over land have not been studied extensively. Based on a patch-mosaic landscape model, we analyzed spatial aggregation changes at two levels corresponding to landscape design during 1949 and 2018. At the landscape level, the global aggregation degree increased initially and then weakened around 2006. However, the spatial aggregation process between dry and wet patterns was inconsistent. For the dry pattern, spatial aggregation was mainly caused by area decline induced decreases in the patch number. For the wet pattern, spatial aggregation was caused by area enlargement induced decreases in the patch number. At the class level, with increases in the dry/wet magnitude, the correlation between the affected area and aggregation strengthened. Our results provide new insights to understand the spatial processes and future trends of dry/wet patterns over land. We argue that future vulnerability of agriculture and ecosystems to drought is likely to be further mediated by the changes in drought patterns' spatial structure.

**Plain Language Summary** Quantifying the spatial variation characteristics of heterogeneous dry/wet patches worldwide can provide an in-depth understanding of regional hydrological regimes. Previous studies have mainly focused on area-based statistics to quantify the changes in the dry/wet patterns, and neglected comprehensive information of the process. Further, whether a long-term spatial aggregation or fragmentation trend exists is also unknown. The patch-mosaic model of landscape ecology provides a new tool to explore this hypothesis at the landscape and class levels. Our results showed that at the landscape level, the global spatial aggregation degree increased initially and then weakened around 2006, including the dry landscape (all dry classes considered together), wet landscape (all wet classes considered together), and total landscape (all classes considered together). At the class level, greater the degree of dryness/wetness, stronger was the correlation between the affected area and aggregation. Our findings provide new insights into identifying the increasing exposure of climate change, which can be used to assess the potential impacts of spatial aggregation or disaggregation of droughts on agriculture and ecosystems, and to predict future changes in the spatial structure of drought patterns.

## 1. Introduction

Extreme events, such as droughts or floods, can disturb regional agriculture, water availability, and ecosystem processes, thereby affecting global human and natural systems (Ault, 2020; Dai, 2011b). Since the 2000s, the increasing frequency of extreme events has affected many areas with high ecological importance (e.g., the Amazon Rainforest; Maeda et al., 2015) and/or high population density (e.g., Northeast China; Yuan et al., 2019). Moreover, future climate change scenarios predict extreme events to increase (Anderegg et al., 2019; Chiang et al., 2021). Along with duration, magnitude, and severity, the spatial extent of events is an essential factor because such events can occupy large areas for extended periods as a regional phenomenon. Changes in spatial extent are the basis for quantitative evaluation of terrestrial and continental dry/wet trends (Scanlon et al., 2018;

© 2022 The Authors.

This is an open access article under the terms of the [Creative Commons Attribution-NonCommercial License](https://creativecommons.org/licenses/by/4.0/), which permits use, distribution and reproduction in any medium, provided the original work is properly cited and is not used for commercial purposes.

**Table 1**  
*Summary of Global Precipitation Data Sets*

Data set <sup>a</sup>	Spatial resolution	Frequency	Coverage	Period	Reference
CRU TS 4.03	0.5° × 0.5°	Monthly	Global land	1901–2018	Harris et al. (2014)
GPCC V2018	0.5° × 0.5°	Monthly	Global land	1901–2016	Rudolf et al. (2005)
PREC/L	0.5° × 0.5°	Monthly	Global land	1948–2011	Chen et al. (2002)
UD V4.01	0.5° × 0.5°	Monthly	Global land	1901–2014	Willmott and Matsuura (1995)
PGF V3	0.25° × 0.25°	Monthly	Global	1948–2016	Sheffield et al. (2006)
CMAP	2.5° × 2.5°	Monthly	Global land	1979–2018	Xie et al. (2007)
GPCP V2.3	2.5° × 2.5°	Monthly	Global	1979–2018	Adler et al. (2003)

<sup>a</sup>CRU TS 4.03, Climatic Research Unit Time-series version 4.03; GPCC V2018, Global Precipitation Climatology Center full data product; PREC/L, National Oceanic & Atmospheric Administration (NOAA) Precipitation Reconstruction over Land; UD V4.01, University of Delaware, version 4.01; PGF V3, Princeton Global Forcings version 3; CMAP, Climate Prediction Center Merged Analysis of Precipitation; GPCP V2.3, Global Precipitation Climatology Center version 2.3.

Sheffield et al., 2012; Spinoni et al., 2018; Xu et al., 2019). However, previous assessments have not completely revealed the structural information hidden in dry/wet patterns.

Identifying and quantifying the spatial continuity of dry/wet events is a promising avenue to complement our understanding of spatial and temporal trends in extreme dry events (Andreadis et al., 2005; Nagarajan, 2009). Several cluster methods have been developed to identify continuous spatial structural changes in large-scale drought events. For example, the severity–area–duration method, first introduced by Andreadis et al. (2005), has been widely used to combine the spatial continuity of individual drought events with their severity (Blanchet & Mélése, 2020; Satish Kumar et al., 2021; Sheffield et al., 2009; Wang et al., 2016). Although these efforts have revealed spatially continuous characteristics of large-scale drought events, the degree of aggregation or fragmentation has not been independently quantified. Furthermore, whether long-term structural changes exist in global dry/wet patterns over land is unclear.

The occurrence of dry/wet events is spatially heterogeneous. In the context of climate change, when small-scale dry/wet patches develop into large-scale patches, the severity can be exacerbated, even if the total area and intensity do not change significantly. However, traditional evaluations of the severity of dry/wet events are usually based on the relationship between duration ( $D$ ) and magnitude ( $M$ ), such as  $D \times M$  or  $D/M$ , which ignore the impact of spatial aggregation. Therefore, exploring the spatial aggregation process on different spatial scales is necessary to widen our understanding of dry/wet events and their potential impacts.

This study aimed to reveal the spatial aggregation changes in the global dry/wet pattern from 1949 to 2018. Owing to the spatial heterogeneity of dry/wet events over land, we adopted a patch-mosaic model of landscape structure to design our framework (McGarigal & Cushman, 2005). First, we calculated the standard precipitation index (SPI) using seven widely used precipitation data sets. Second, we divided the SPI into nine dry/wet types in each grid box. Third, landscape aggregation metrics were applied to quantify spatial aggregation changes at the landscape level, including the dry (all dry classes considered together), wet (all wet classes considered together), and total landscapes (all classes considered together). Fourth, we further explored the relationship between area and aggregation at the class level of the SPI. Additionally, we revealed heterogeneous aggregation characteristics at the landscape level on different zonal and temporal scales. Finally, the temporal effect of spatial aggregation in the global dry/wet pattern was explored based on the Climatic Research Unit (CRU) data set. Our characterization of aggregation changes in the dry/wet pattern will provide an in-depth understanding of the potential impacts of dry/wet events.

## 2. Data and Methods

### 2.1. Precipitation Data Sets

Multi-source precipitation products were used to reduce the uncertainty or error analysis owing to the irregular spatial distribution of observation stations worldwide (Sun et al., 2018; Trenberth, 2011; Trenberth et al., 2014). Considering the robustness of the spatial analysis, we collected seven common global precipitation products

**Table 2**  
*Classifications of the Standard Precipitation Index (SPI; Hänsel et al., 2016)*

Category	SPI value	Name
W4	$\geq 2.00$	Extremely wet
W3	1.50–1.99	Severely wet
W2	1.00–1.49	Moderately wet
W1	0.50–0.99	Mild wet
NN	–0.49–0.49	Near normal
D1	–0.99–(–0.50)	Mild dry
D2	–1.49–(–1.00)	Moderately dry
D3	–1.99–(–1.50)	Severely dry
D4	$\leq -2.00$	Extremely dry

to conduct a landscape analysis. These precipitation data sets, which are established and widely used (Table 1), were collected from the CRU, Global Precipitation Climatology Center (GPCC), National Oceanic & Atmospheric Administration (NOAA), Precipitation Reconstruction over Land (PREC/L), University of Delaware (UD), Princeton Global Forcings (PGF), Climate Prediction Center Merged Analysis of Precipitation (CMAP), and monthly precipitation data set of the Global Precipitation Climatology Project (GPCP). Using the bilinear interpolation method, all the precipitation data were rescaled to a spatial resolution of  $0.5^\circ$ , on a monthly scale. Considering the lack of global observation stations before the 1950s and the temporal consistency of different data sets, our analysis was conducted between 1948 and 2018. However, PREC/L, PGF, GPCC, and UD were not included for the 2012–2018 analysis, owing to their unavailability.

The CRU Time Series 4.03 precipitation data set, which provides monthly data with a spatial resolution of  $0.5^\circ \times 0.5^\circ$  over global land (1901–2018), was based on near-surface measurements and was cross-validated at the station level. These homogeneous records provide reliable temporal trends of

the CRU data sets (Harris et al., 2020; Hopping et al., 2018; Sun et al., 2018); additionally, they have been widely used for analyzing climate variability and assessment of Earth system models. In this study, the CRU precipitation data set was used to analyze the temporal scale effects among the seven data sets. The GPCC full data product (V2018), with a resolution of  $0.5^\circ$  and period of 1901–2016, was developed from more than 70,000 stations worldwide. It has excellent performance for the verification of climate models, analysis of historic precipitation worldwide, and research on global and regional water cycles (Rudolf et al., 2005). The NOAA PREC/L data set is mainly collected from the Global Historical Climatology Network version 2 (GHCN2) and the Climate Anomaly Monitoring System (Chen et al., 2002), including more than 17,000 stations since 1948. The UD precipitation product V4.01 is mainly acquired from GHCN2 and more widely from the archive of Legates and Willmott (Willmott & Matsuura, 1995). The data set covers a period of 1900–2014 and is limited to land, which complements the International Comprehensive Ocean–Atmosphere data set. The PGF version 3 combines observations and reanalysis data to generate global and long-term (1948–2016) precipitation data (Sheffield et al., 2006). The CMAP monthly data set is generated based on multiple types of satellite estimates and gauge data, spanning the period since 1979 (Xie et al., 2007). The GPCP product provides reliable global precipitation by integrating various global satellite data sets. Specifically, data were collected from rain gauge stations, satellites, and sounding observations and span 1979 to the present. A careful combination of satellite-based rainfall estimates provides the necessary spatial structural details for landscape analysis (Adler et al., 2003).

## 2.2. SPI

Many indices have been developed for monitoring surface drought variability at different spatial scales, including the Palmer drought severity index (PDSI) (Dai, 2011a), the self-calibrated PDSI (scPDSI) (van der Schrier et al., 2013), and the standardized precipitation evapotranspiration index (SPEI) (Vicente-Serrano et al., 2010). However, these indicators are mainly based on the water balance equation, which needs to incorporate the surface evaporation demand. The calculation of evaporation demand usually relies on the Penman–Monteith formula (Dai & Zhao, 2017; Milly & Dunne, 2016). P–M-based potential evaporation not only considers the influence of wind, humidity, solar, and radiation variables, but also the observation data of these variables, which are not easy to obtain at a global scale and show evident temporal and spatial heterogeneity. Considering the spatial uncertainty of the spatial index itself, which struggles to account for variations in wind speed, radiation, and humidity (Dai & Zhao, 2017; Milly & Dunne, 2016; Yang et al., 2018), we elected to use SPI, which is based only on the precipitation probabilistic approach to conduct a spatial structured analysis of dry and wet patterns (McKee et al., 1993). Nevertheless, we also found a similar trend using the published scPDSI data set (Figure S1 in Supporting Information S1).

SPI is the degree of the standardized deviation of the empirical precipitation probability distribution function (Hayes et al., 1999). It allows the evaluation of the impact of precipitation anomalies of a single model in different geographical locations and makes spatial comparisons on multiple timescales. SPI can be calculated on different

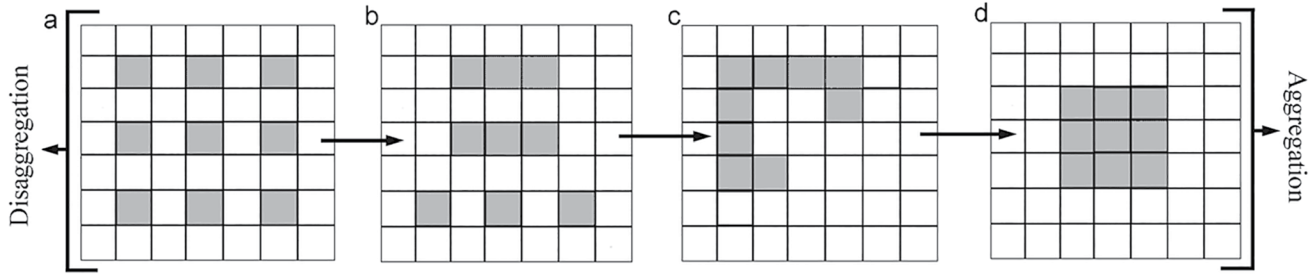


**Figure 1.** Set of binary landscape maps represented by  $7 \times 7$  grids. Each grid contains 40 white cells and 9 black cells. The spatial distribution of the black cells starts from a dispersed square patch (Figure 1a). The black cells are gradually aggregated (Figures 1b–1d). In this landscape, the largest patch square is  $7 \times 7$  grids; thus,  $m = 11$ ,  $n = 7$ , and that the  $\max_{g_{i,j}} = 104$ . Following Equation 4, the AIs of Figures 1a–1d are 0, 0.333, 0.917, and 1.0, respectively. From the above landscape patterns, AI is sensitive to total area and the number of patches.

timescales to explain spatial dry and wet changes on monthly to multi-year scales. In this study, we divided the annual average SPI maps into nine categories (Table 2) to define spatially heterogeneous levels and to quantify spatial structured changes. Additionally, we used the 3, 6, 12, 24, and 48-month SPI to evaluate the short-term and long-term temporal effects. A timescale of 12 months is recommended to conduct landscape aggregation analysis of the global dry/wet pattern between 1949 and 2018 (Haile et al., 2020). Truncating the annual SPI variability into dry/wet classes still compromised the structural integrity of continuously varying attributes. To some extent, this led to spatial information loss and increased uncertainty.

### 2.3. Landscape Structure Metrics

Under the patch-mosaic paradigm, different closed dry/wet patches are the most common composition of landscape patterns (McGarigal & Cushman, 2005). Specifically, dry/wet patches refer to geographic areas with relatively stable moisture conditions, while global dry/wet landscape is denoted as a collection of discrete dry/wet patches with different thresholds of SPI. Thus, the degree of spatial aggregation was determined by the spatial distribution of these dry/wet patches. This study mainly used an aggregation index (AI) to measure spatial aggregation changes. Additionally, the total area (TA) and number of patches (NP) corresponding to different dry/wet classes or landscapes were used to interpret the mechanisms of spatial structural changes.

The AI is calculated based on an adjacency matrix that shows the frequency of different pairs of patch types appearing side-by-side in the maps. If  $g_{i,j}$  represents the total edges of type  $i$  adjacent to type  $j$ , for type  $i$  of area  $A_i$ , the AI measures  $g_{i,j}$ , and the total edges are shared by type  $i$  itself. Shared edges were counted using a single counting method, where each pixel edge was counted only once. Given a type  $i$  of area  $A_i$ , the maximum aggregation level is reached when the patch type is a single patch that has the largest  $g_{i,j}$ . If  $n$  is the side of the largest integer, a square smaller than  $A_i$ , and  $m = A_i - n^2$ , the largest number of shared edges for type  $i$ ,  $\max_{g_{i,j}}$ , will take one of the following forms:

$$\max_{g_{i,j}} = 2n(n - 1), \quad \text{when } m = 0, \text{ or} \quad (1)$$

$$\max_{g_{i,j}} = 2n(n - 1) + 2m - 1, \quad \text{when } m < n, \text{ or} \quad (2)$$

$$\max_{g_{i,j}} = 2n(n - 1) + 2m - 2, \quad \text{when } m \geq n. \quad (3)$$

The maximum level of the AI for type  $i$  is calculated as  $\max_{g_{i,j}}/A_i$ , and the AI for type  $i$  is derived as follows:

$$AI_i = g_{i,j} / \max_{g_{i,j}} \quad (4)$$

Therefore,  $AI_i$  ranges from 0 to 1. When  $AI_i = 1$ , the patch type is aggregated to the maximum ( $g_{i,j} = \max_{g_{i,j}}$ ; Figure 1a) and  $AI_i$  is 0 when  $g_{i,j}$  reaches the minimum ( $g_{i,j} = 0$ ; Figure 1d). For the overall spatial range,  $AI_L$  can be calculated by coupling  $AI_i$  weighted by  $P_i$  as follows:

$$AI_L = \sum_{i=1}^n AI_i \times p_i \quad (5)$$

where  $n$  is the total number of climatic types and  $P_i$  is the percentage of  $A_i$ .

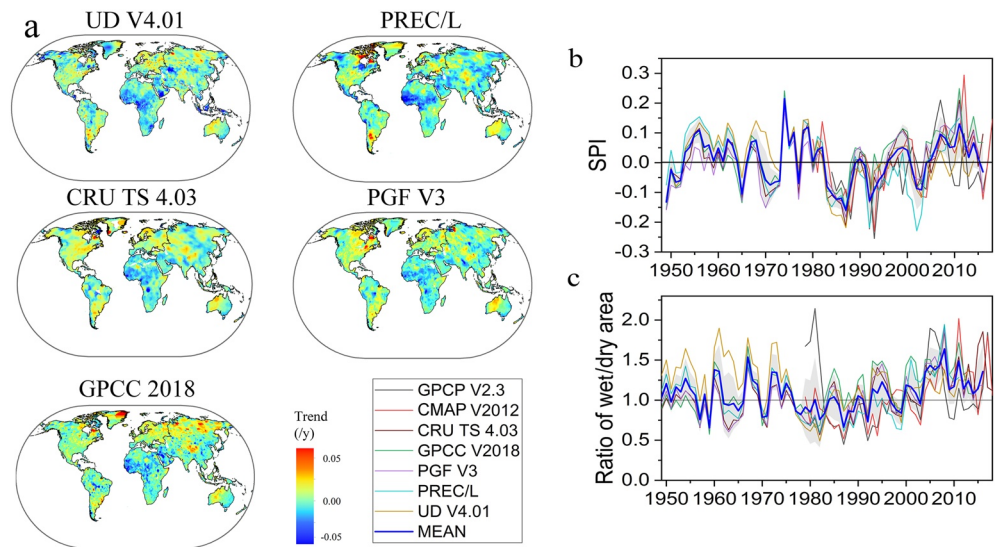


**Figure 2.** (a) Standard precipitation index (SPI) trends, (b) time series, and (c) ratios of wet (SPI > 0.5) and dry (SPI < -0.5) areas from 1948 to 2018 based on the seven data sets. Blue lines represent the average of the data sets; the gray area denotes  $\pm 1$  standard deviation (s.d.). Abbreviations: CRU TS 4.03, Climatic Research Unit Time-series version 4.03; GPCP V2018, Global Precipitation Climatology Center full data product; PREC/L, National Oceanic & Atmospheric Administration (NOAA) Precipitation Reconstruction over Land; UD V4.01, University of Delaware version 4.01; PGF V3, Princeton Global Forcings version 3; CMAP, Climate Prediction Center Merged Analysis of Precipitation; GPCP V2.3, Global Precipitation Climatology Center version 2.3.

## 2.4. Statistical Analysis

Owing to the large spatial heterogeneity and uncertainty of precipitation data sets, the Z-score transformation method was adopted to standardize the variables derived from multiple precipitation data sets (Cheadle et al., 2003). Z-scores are calculated by subtracting the overall average from the raw data and dividing the result by their standard deviation. Through this method, the structural changes in the landscape derived from different data sets can be effectively evaluated. Furthermore, we applied the non-parametric Mann-Kendall (M-K) statistical test to assess the statistical significance of the temporal trends (Kendall, 1975; Mann, 1945). The M-K significance test is less affected by missing values and uneven distribution than other tests (Yue et al., 2002). Additionally, Pearson's correlation coefficient ( $r$ ) was used to examine the statistical relationships between the different variables.

## 3. Results

### 3.1. Area-Based Changes in the Global Dry/Wet Patterns

Figure 2a shows the spatial dry/wet trends of SPI from 1948 to 2018, excluding GPCP and CMAP for short periods. Specifically, substantial spatial differences were observed between the drying and wetting distributions, particularly in areas with upward trends in mid-high latitude regions (30°–75°), such as Europe, North Asia, South America, and West Australia. Conversely, downward trends occurred in Africa, northern parts of South America, and East Asia. Over time, the global average SPI increased, particularly since the 1980s. A downward trend around 2006 was most probably caused by an increasing number of El Niño/Southern Oscillations (ENSOs) from the 1980s to 2006 (Figure 2b), which are considered to be the main sources of changes in global precipitation records (Ault, 2020; Huang et al., 2019; Yeh et al., 2018). The ratios of wet (SPI > 0.5) and dry (SPI < -0.5) areas rapidly increased global humidity since the 1980s compared to the 1950–1980s (Figure 2c). Overall, from the 1980s to 2006, global wetting trends were common in mid-high latitudes, while Africa, East Asia, and the Amazon exhibited prominent drying trends.

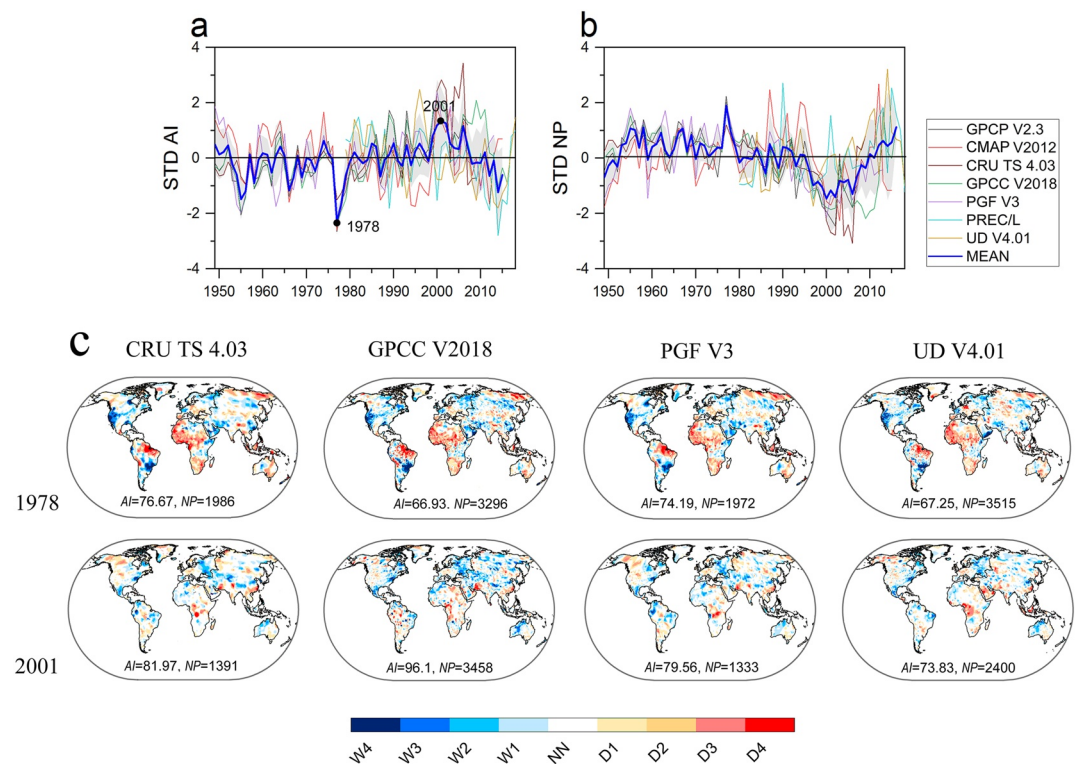


**Figure 3.** Temporal changes of (a) the standardized aggregation index (AI) and the (b) number of patches (NP) in global dry/wet landscape patterns (all classes considered together). Dashed color lines represent different data sets; blue solid lines represent the arithmetic mean of different data sets; the gray area denotes  $\pm 1$  standard deviation (s.d.). (c) Maps of dry/wet classes in 1978 and 2001 based on the Climatic Research Unit (CRU), Global Precipitation Climatology Center (GPCC), Princeton Global Forcings (PGF), and University of Delaware (UD) data sets. All closed areas are designed as dry/wet patches with different standard precipitation index (SPI) levels.

### 3.2. Aggregation Changes at the Landscape Level

Figures 3a and 3b show that global AI (all classes considered together) increased rapidly from the 1980s, before exhibiting a downward trend around 2006 (Z-score). NP and AI changes showed opposite trends. In the context of a constant global area, changes in spatial aggregation are likely to be determined by changes in the number of wet and dry patches. From the 1980s until 2006, the reduction of dry patches and the combination of wet patches most probably increased spatial aggregation. We considered the minimum global AI in 1978 and maximum global AI in 2001 as examples to illustrate the spatial aggregation changes (Figure 3c). Although spatial heterogeneity in different data sets was large, we found a clear spatial aggregation process, in which the AI increased while NP decreased in different data sets. Generally, between 1978 and 2001, the number of dry patches in Africa and South America decreased significantly, which likely enhanced the global spatial aggregation degree.

Figure 4 shows the changes in AI in dry patterns (all dry classes considered together) and wet patterns (all wet classes considered together) from 1949 to 2018 (Z-score). Generally, the increases in AI between dry and wet patterns were consistent in all the analyzed data sets and their trends were inverted around 2006. However, the increasing rates of AI in wet patterns were almost 10 times higher than those of AI in dry patterns. Furthermore, the dry and wet patterns showed evident differences. In the dry patterns, changes in AI (Figure 4a) were consistent with TA (Figure 4b) and NP (Figure 4c) changes, suggesting that a simultaneous decrease in dry area and the number of patches relatively increased AI. In contrast, in the wet patterns, changes in AI (Figure 4d) were consistent with TA changes (Figure 4e), but contrary to NP changes (Figure 4f), suggesting that the increase in AI was caused by the decrease in the number of wet patches due to the expansion of the wet area. Overall, although there are different mechanisms responsible for AI changes, the spatial aggregation variations in the wet and dry patterns increased from the 1980s until 2006, and subsequently, weakened.

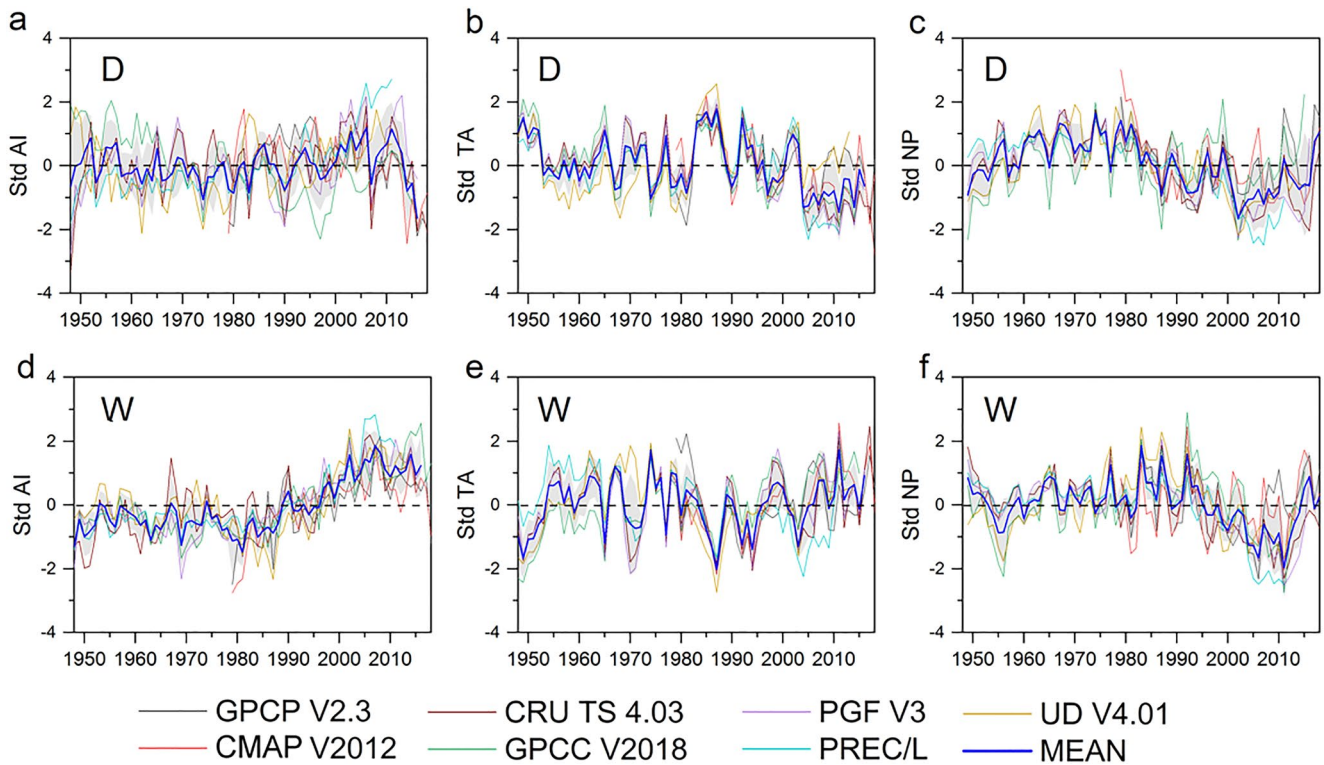


**Figure 4.** Temporal changes in the (a and d) standardized aggregation index (AI), (b and e) total area (TA), and (c and f) number of patches (NP) between dry patterns and wet patterns from 1949 to 2018 (dry and wet classes considered respectively). Color dashed lines represent different data sets; the blue solid lines represent the arithmetic mean of different data sets; the gray area denotes  $\pm 1$  standard deviation (s.d.). Symbols “D” and “W” represent dry and wet patterns, respectively.

### 3.3. Aggregation Changes at Class Level

As summarized in Table 3, temporal trends in TA were not in equilibrium with those in AI, based on different dry/wet classes. Specifically, the TA of dry classes decreased clearly, while that of wet classes weakly increased. The trends of mild dry (D1) and moderately dry (D3) were  $-0.042\%/y$  and  $-0.025\%/y$  ( $p < 0.01$ , M–K), respectively. In contrast, the changes in AI in wet classes increased. In particular, the AI changes of the wet classes (W1–W3) were statistically significant, with the respective rates being  $0.018\%/y$ ,  $0.027\%/y$ , and  $0.028\%/y$  ( $p < 0.01$ , M–K). Figure 5 shows a generally significant correlation between the TA and AI at the class level. With an increase in dry/wet levels, the correlations increased. In the D1 and W1 classes, the  $r$  between the TA and AI was weak. Usually, when drought/floods occur mildly, the affected drought area was usually large, and the distribution was discrete. Conversely, in the D4 and W4 classes,  $r$  was  $>0.7$  in the GPCP and UD data sets. When severe droughts and floods occurred, the spatial extent was relatively small and aggregated.

### 3.4. Aggregation Changes at Zonal Scale

Figure 6 shows the temporal changes of AI, TA, and NP in the zones of  $30^{\circ}\text{S}$ – $30^{\circ}\text{N}$  and  $30^{\circ}$ – $90^{\circ}\text{N}$  (Z-score). In general, changes in AI in both zones showed an increasing trend since the 1980s, followed by a downward trend around 2006. However, different response mechanisms may exist in the affected area in different dry/wet patterns

**Table 3**  
Linear Trends of Total Area (TA) and Aggregation Index (AI) at the Class Level

Class	W4	W3	W2	W1	NN	D1	D2	D3	D4
AI	0.004	<b>0.018**</b>	<b>0.027**</b>	<b>0.028**</b>	<b>0.031**</b>	<b>0.012*</b>	0.003	−0.001	0.007
TA	−0.001	0.002	0.007	0.004	<b>0.058**</b>	<b>−0.042**</b>	<b>−0.025**</b>	−0.007	0.001

Note. \*\*and \* represents 0.05 and 0.01 significance of the Mann–Kendall (M–K) statistical test.



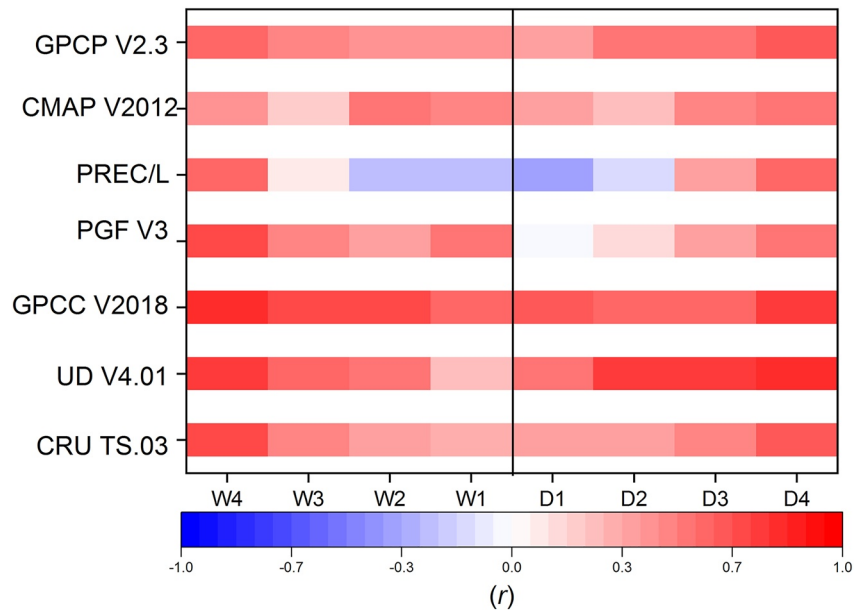


**Figure 5.** Correlation  $r$  between total area (TA) and aggregation index (AI) between 1949 and 2018, at class level. Abbreviations: CRU TS 4.03, Climatic Research Unit Time-series version 4.03; GPCC V2018, Global Precipitation Climatology Center full data product; PREC/L, National Oceanic & Atmospheric Administration (NOAA) Precipitation Reconstruction over Land; UD V4.01, University of Delaware version 4.01; PGF V3, Princeton Global Forcings version 3; CMAP, Climate Prediction Center Merged Analysis of Precipitation; GPCP V2.3, Global Precipitation Climatology Center version 2.3.

and zones. Between  $30^\circ$  and  $30^\circ\text{N}$ , changes in AI in dry and wet patterns were consistent with the changes in TA and NP. This was likely attributable to El Niño, which frequently decreases precipitation over many low-latitude land areas (Ault, 2020; J. Zhang et al., 2021; W. Zhang et al., 2019). This caused a shift toward a relative aggregation phenomenon due to the disappearance of dry and wet patches. In contrast, between  $30^\circ$  and  $90^\circ\text{N}$ , changes in AI in dry patterns were different from those in low-latitude regions. The decreasing area reduced the number of patches, which increased the spatial aggregation. In their wet patterns, changes in AI were consistent with those in TA, but opposite to NP (Figures 6d, 6h and 6l). The increase in the degree of spatial aggregation could be attributed to the expansion and combination in wet areas, which decreased the number of patches. Particularly since the 1980s, precipitation on land has been controlled by ENSO with more La Niña phases and more large-scale rain events in high-latitude zones (Domeisen et al., 2019; Grothe et al., 2020; Trenberth et al., 2014). However, around 2006, the changes in the AI of the different zones could be attributed to the decline of La Niña events on land.

### 3.5. Temporal Changes in Aggregation

Different timescales reflect the impact of spatial aggregation of water resource availability. Figure 7a shows the time-series of global AI over 3 to 48-month timescales. For the 3-month time-scale, AI increased from 93.5% to 94%. For the 48-month timescale, AI increased from 83.5% to 83.8%. In general, longer the timescale, lower is the degree of aggregation. Furthermore, Figure 7b indicates an apparent difference in the linear trends for the 3 to 48-month timescales. Specifically, over periods of less than 12 months, spatial aggregation increased rapidly, and then stabilized. Figure 7c further illustrates the global drought patterns on 3 to 48-month timescales in 2004. In general, the spatial aggregation decreased from 94.81% to 85.72%, and the spatial distribution of dry/wet patches tended to be stable for timescales of more than 12 months. Generally, longer the timescales, more stable is the spatial aggregation status. This further suggested that longer the duration of aggregation, greater is the severity of extreme events.

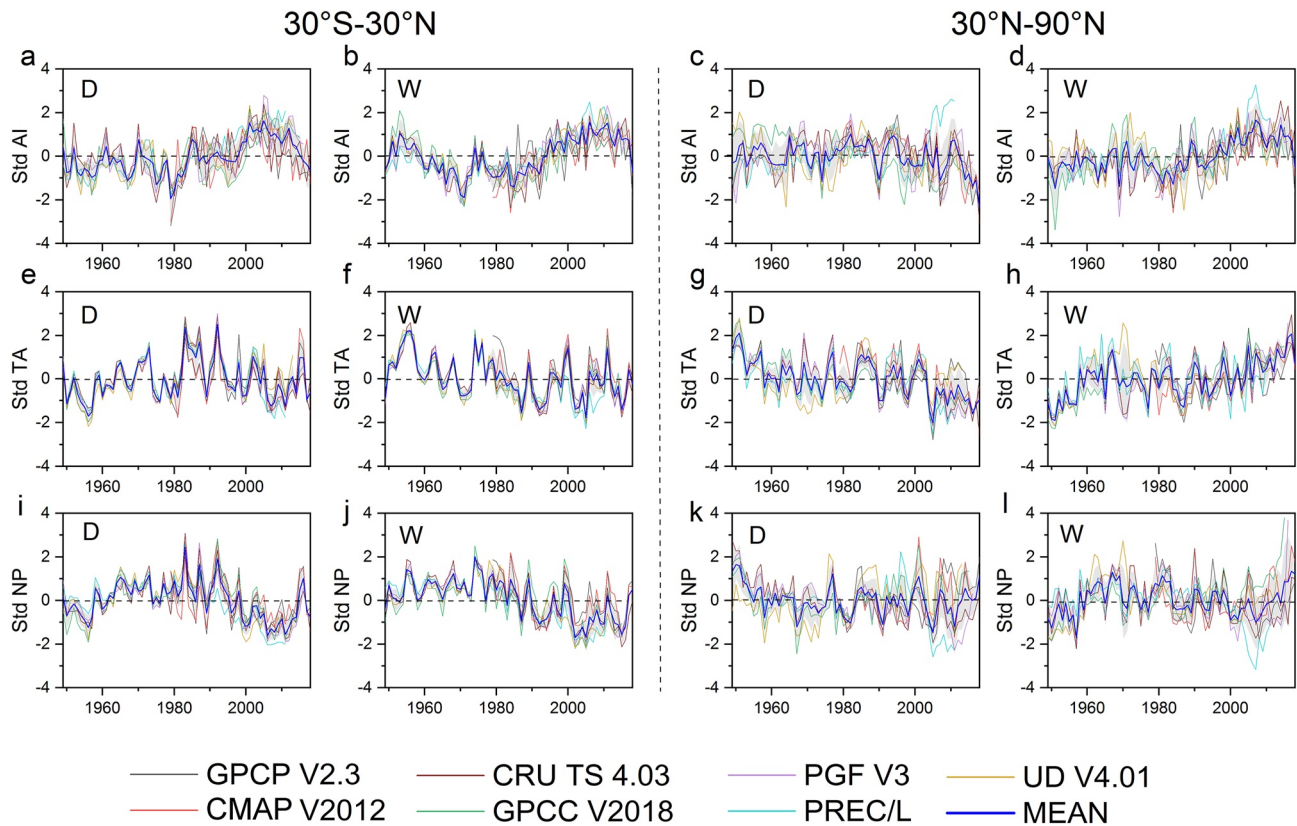


**Figure 6.** Temporal changes in the (a–c) standardized aggregation index (AI), (e–h) total area (TA), and (i–l) number of patches (NP) in dry and wet patterns in the zones between 30°S–30°N and 30°–90°N (dry and wet classes considered respectively). Dashed color lines represent different data sets; blue solid lines represent the arithmetic mean of different data sets and the gray area denotes  $\pm 1$  standard deviation (s.d.). Symbols “D” and “W” represent dry and wet patterns, respectively.

#### 4. Conclusions

Owing to the patch characteristic of dry/wet patterns, a simplified patch-mosaic framework was designed to characterize spatial structural characteristics based on multiple precipitation data sets. In the context of climate change, our results showed an obvious global wetting trend since the 1980s. We identified an evident global aggregation increase at the different landscape levels, including all classes (wet and dry) considered together from the 1980s to 2006. However, the mechanisms between the dry and wet patterns were not consistent. In the dry patterns, the reduction of area and number of patches increased the spatial aggregation, whereas in the wet patterns, the expansion of the area reduced the number of patches and increased the spatial aggregation. Thereafter, at the class level, the correlations between spatial aggregation and total area increased with an increase in dry/wet levels. Additionally, at the zonal scale, the changes in spatial aggregation also showed different processes in low- and high-latitude zones.

The occurrence of ENSO events is likely to cause changes in the spatial structure of global dry/wet patterns (Figure S2 in Supporting Information S1), which are closely related to the formation of global hydrological regimes. Numerous moisture budgeting experiments have revealed the key dynamics of these teleconnections. For example, the equator-ward propagation of winter storms during El Niño years can alter the moisture transport through deep convection. This could cause widespread droughts in the Pacific Northwest, leading not only to an increase in the total area of drought patterns, but also potentially an increase in the spatial aggregation degree. In future global warming scenarios, there is high confidence that the extreme events associated with ENSO will increase, and the compound effects of climate change and spatial aggregation on dry/wet events may be further enhanced. Additionally, the results of landscape analysis are highly sensitive to the selected spatial resolution, as statistical relationships may change with spatial resolution. Specifically, using coarse resolution data would weaken the spatial heterogeneity; conversely, finely resolved data would detect more small-scale features, making the climatic features disordered, requiring further extensive research.

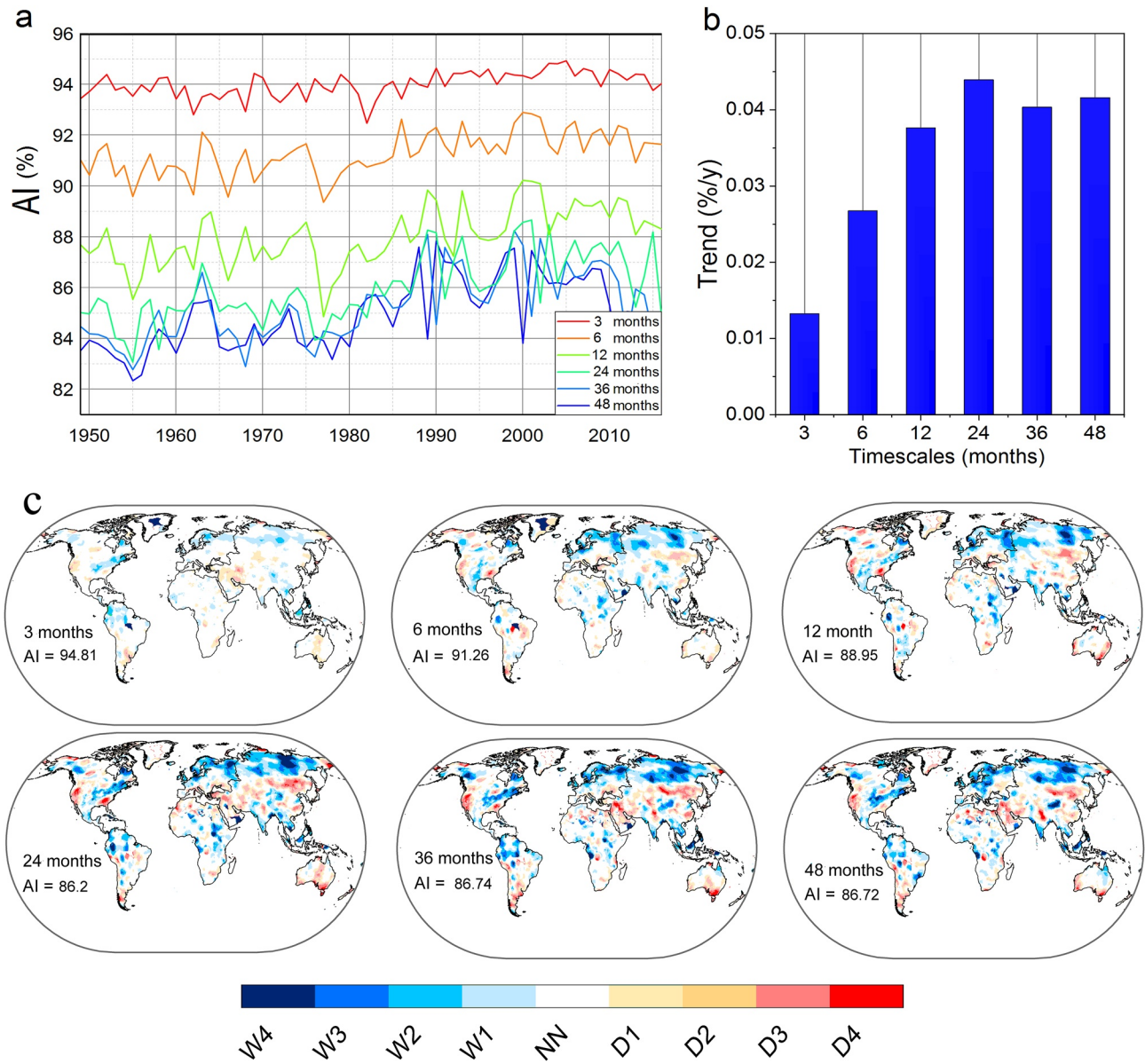


**Figure 7.** (a) Temporal changes and (b) linear trends in the aggregation index on 3, 6, 12, 24, 36, and 48-month timescales between 1949 and 2018 based on Climatic Research Unit (CRU) data sets. (c) Maps of the standard precipitation index (SPI) over 3, 6, 12, 24, 36 and 48-month timescales in 2004 based on the CRU data sets.

### Data Availability Statement

The data used in this study were published open access and are available on NOAA Physical Laboratory Sciences via <https://psl.noaa.gov/data/gridded/tables/precipitation.html>. In this study, our data is freely available at the Mendeley via DOI <https://doi.org/10.17632/f2wrkdbp5x.1>.

### Acknowledgments

This study has been supported by the National Natural Science Foundation of China (grant no. 41625001), the Strategic Priority Research Program of the Chinese Academy of Sciences (grant no. XDA20060402), the High-level Special Funding of the Southern University of Science and Technology (Grant no. G02296302, G02296402), the Pengcheng Scholar Program of Shenzhen, the National High-level Talents Special Support Plan (“Ten Thousand Talents Plan”), and the Leading Innovative Talent Program for young and middle-aged scholars by the Ministry of Science and Technology. E.E. Maeda was funded by the Academy of Finland (Grant no. 318252, 319905 and 345472). We are particularly grateful to the two anonymous reviewers and Dr. Olga Hannonen for their useful comments on the manuscript.

### References

- Adler, R. F., Huffman, G. J., Chang, A., Ferraro, R., Xie, P. P., Janowiak, J., et al. (2003). The version-2 global precipitation climatology project (GPCP) monthly precipitation analysis (1979–present). *Journal of Hydrometeorology*, 4(6), 1147–1167. [https://doi.org/10.1175/1525-7541\(2003\)004<1147:TVGPCP>2.0.CO;2](https://doi.org/10.1175/1525-7541(2003)004<1147:TVGPCP>2.0.CO;2)
- Anderegg, W. R. L., Trugman, A. T., Bowling, D. R., Salvucci, G., & Tuttle, S. E. (2019). Plant functional traits and climate influence drought intensification and land–atmosphere feedbacks. *Proceedings of the National Academy of Sciences*, 116(28), 14071–14076. <https://doi.org/10.1073/pnas.1904747116>
- Andreadis, K. M., Clark, E. A., Wood, A. W., Hamlet, A. F., & Lettenmaier, D. P. (2005). Twentieth-century drought in the conterminous United States. *Journal of Hydrometeorology*, 6(6), 985–1001. <https://doi.org/10.1175/JHM450.1>
- Ault, T. R. (2020). On the essentials of drought in a changing climate. *Science*, 368(6489), 256–260. <https://doi.org/10.1126/SCIENCE.ABC4034>
- Blanchet, J., & Mélése, V. (2020). A Bayesian framework for the multiscale assessment of storm severity and related uncertainties. *Journal of Hydrometeorology*, 21(1), 109–122. <https://doi.org/10.1175/JHM-D-18-0254.1>
- Cheadle, C., Vawter, M. P., Freed, W. J., & Becker, K. G. (2003). Analysis of microarray data using Z score transformation. *Journal of Molecular Diagnostics*, 5(2), 73–81. [https://doi.org/10.1016/S1525-1578\(10\)60455-2](https://doi.org/10.1016/S1525-1578(10)60455-2)
- Chen, M., Xie, P., Janowiak, J. E., & Arkin, P. A. (2002). Global land precipitation: A 50-yr monthly analysis based on gauge observations. *Journal of Hydrometeorology*, 3(3), 249–266. [https://doi.org/10.1175/1525-7541\(2002\)003](https://doi.org/10.1175/1525-7541(2002)003)
- Chiang, F., Mazdiyasi, O., & AghaKouchak, A. (2021). Evidence of anthropogenic impacts on global drought frequency, duration, and intensity. *Nature Communications*, 12(1), 1–10. <https://doi.org/10.1038/s41467-021-22314-w>
- Dai, A. (2011a). Characteristics and trends in various forms of the Palmer Drought Severity Index during 1900–2008. *Journal of Geophysical Research*, 116(12), D12115. <https://doi.org/10.1029/2010JD015541>
- Dai, A. (2011b). Drought under global warming: A review. *Wiley Interdisciplinary Reviews: Climate Change*, 2(1), 45–65. <https://doi.org/10.1002/wcc.81>
- Dai, A., & Zhao, T. (2017). Uncertainties in historical changes and future projections of drought. Part I: Estimates of historical drought changes. *Climatic Change*, 144(3), 519–533. <https://doi.org/10.1007/s10584-016-1705-2>
- Domeisen, D. I. V., Garfinkel, C. I., & Butler, A. H. (2019). The teleconnection of El Niño Southern Oscillation to the stratosphere. *Reviews of Geophysics*, 57(1), 5–47. <https://doi.org/10.1029/2018RG000596>
- Grothe, P. R., Cobb, K. M., Liguori, G., Di Lorenzo, E., Capotondi, A., Lu, Y., et al. (2020). Enhanced El Niño–Southern oscillation variability in recent decades. *Geophysical Research Letters*, 47(7), 1–8. <https://doi.org/10.1029/2019GL083906>
- Haile, G. G., Tang, Q., Hosseini-Moghari, S. M., Liu, X., Gebremicael, T. G., Leng, G., et al. (2020). Projected impacts of climate change on drought patterns over East Africa. *Earth's Future*, 8(7), 1–23. <https://doi.org/10.1029/2020EF001502>
- Hänsel, S., Schucknecht, A., & Matschullat, J. (2016). The Modified Rainfall Anomaly Index (mRAI)—Is this an alternative to the Standardised Precipitation Index (SPI) in evaluating future extreme precipitation characteristics? *Theoretical and Applied Climatology*, 123(3–4), 827–844. <https://doi.org/10.1007/s00704-015-1389-y>
- Harris, I., Jones, P. D., Osborn, T. J., & Lister, D. H. (2014). Updated high-resolution grids of monthly climatic observations—The CRU TS3.10 Dataset. *International Journal of Climatology*, 34(3), 623–642. <https://doi.org/10.1002/joc.3711>
- Harris, I., Osborn, T. J., Jones, P., & Lister, D. (2020). Version 4 of the CRU TS monthly high-resolution gridded multivariate climate dataset. *Scientific Data*, 7(1), 1–18. <https://doi.org/10.1038/s41597-020-0453-3>
- Hayes, M. J., Svoboda, M. D., Wilhite, D. A., & Vanyarkho, O. V. (1999). Monitoring the 1996 drought using the standardized precipitation index. *Bulletin of the American Meteorological Society*, 80(3), 429–438. [https://doi.org/10.1175/1520-0477\(1999\)080](https://doi.org/10.1175/1520-0477(1999)080)
- Hopping, K. A., Yeh, E. T., Gaerrang, & Harris, R. B. (2018). Linking people, pixels, and pastures: A multi-method, interdisciplinary investigation of how rangeland management affects vegetation on the Tibetan Plateau. *Applied Geography*, 94, 147–162. <https://doi.org/10.1016/j.apgeog.2018.03.013>
- Huang, S., Wang, L., Wang, H., Huang, Q., Leng, G., Fang, W., & Zhang, Y. (2019). Spatio-temporal characteristics of drought structure across China using an integrated drought index. *Agricultural Water Management*, 218, 182–192. <https://doi.org/10.1016/j.agwat.2019.03.053>
- Kendall, M. G. (1975). *Rank correlation methods*. Griffin.
- Maeda, E. E., Kim, H., Aragão, L. E. O. C., Famiglietti, J. S., & Oki, T. (2015). Disruption of hydroecological equilibrium in southwest Amazon mediated by drought. *Geophysical Research Letters*, 42(18), 7546–7553. <https://doi.org/10.1002/2015GL065252>
- Mann, H. B. (1945). Nonparametric tests against trend. *Econometrica: Journal of the Econometric Society*, 13(3), 245–259. <https://doi.org/10.2307/1907187>
- McGarigal, K., & Cushman, S. A. (2005). The gradient concept of landscape structure. *Issues and Perspectives in Landscape Ecology*, 112–119. <https://doi.org/10.1017/CBO9780511614415.013>
- McKee, T. B., Doesken, N. J., & Kleist, J. (1993). The relation of drought frequency and duration to time scales. In *Proceedings of the 8th Conference on Applied Climatology* (pp. 179–184). American Meteorological Society.
- Milly, P. C. D., & Dunne, K. A. (2016). Potential evapotranspiration and continental drying. *Nature Climate Change*, 6(10), 946–949. <https://doi.org/10.1038/nclimate3046>
- Nagarajan, R. (2009). Drought indices. In *Drought assessment* (pp. 160–204). John Wiley & Sons, Inc. [https://doi.org/10.1007/978-90-481-2500-5\\_5](https://doi.org/10.1007/978-90-481-2500-5_5)
- Rudolf, B., Beck, C., Grieser, J., & Schneider, U. (2005). *Global precipitation analysis products of the GPCC* (pp. 1–8). Internet Publication. Retrieved from [ftp://ftp-anon.dwd.de/pub/data/gpcc/PDF/GPCC\\_intro\\_products\\_2008.pdf](ftp://ftp-anon.dwd.de/pub/data/gpcc/PDF/GPCC_intro_products_2008.pdf)
- Satish Kumar, K., AnandRaj, P., Sreelatha, K., & Sridhar, V. (2021). Regional analysis of drought severity-duration-frequency and severity-area-frequency curves in the Godavari River Basin, India. *International Journal of Climatology*, 41(12), 5481–5501. <https://doi.org/10.1002/joc.7137>
- Scanlon, B. R., Zhang, Z., Save, H., Sun, A. Y., Schmied, H. M., Van Beek, L. P. H., et al. (2018). Global models underestimate large decadal declining and rising water storage trends relative to GRACE satellite data. *Proceedings of the National Academy of Sciences of the United States of America*, 115(6), E1080–E1089. <https://doi.org/10.1073/pnas.1704665115>
- Sheffield, J., Andreadis, K. M., Wood, E. F., & Lettenmaier, D. P. (2009). Global and continental drought in the second half of the twentieth century: Severity-area-duration analysis and temporal variability of large-scale events. *Journal of Climate*, 22(8), 1962–1981. <https://doi.org/10.1175/2008JCLI2722.1>
- Sheffield, J., Goteti, G., & Wood, E. F. (2006). Development of a 50-year high-resolution global dataset of meteorological forcings for land surface modeling. *Journal of Climate*, 19(13), 3088–3111. <https://doi.org/10.1175/JCLI3790.1>
- Sheffield, J., Wood, E. F., & Roderick, M. L. (2012). Little change in global drought over the past 60 years. *Nature*, 491(7424), 435–438. <https://doi.org/10.1038/nature11575>

- Spinoni, J., Vogt, J. V., Naumann, G., Barbosa, P., & Dosio, A. (2018). Will drought events become more frequent and severe in Europe? *International Journal of Climatology*, 38(4), 1718–1736. <https://doi.org/10.1002/joc.5291>
- Sun, Q., Miao, C., Duan, Q., Ashouri, H., Sorooshian, S., & Hsu, K. L. (2018). A review of global precipitation data sets: Data sources, estimation, and intercomparisons. *Reviews of Geophysics*, 56(1), 79–107. <https://doi.org/10.1002/2017RG000574>
- Trenberth, K. E. (2011). Changes in precipitation with climate change. *Climate Research*, 47(1–2), 123–138. <https://doi.org/10.3354/cr00953>
- Trenberth, K. E., Dai, A., Van Der Schrier, G., Jones, P. D., Barichivich, J., Briffa, K. R., & Sheffield, J. (2014). Global warming and changes in drought. *Nature Climate Change*, 4(1), 17–22. <https://doi.org/10.1038/nclimate2067>
- van der Schrier, G., Barichivich, J., Briffa, K. R., & Jones, P. D. (2013). A scPDSI-based global data set of dry and wet spells for 1901–2009. *Journal of Geophysical Research: Atmospheres*, 118(10), 4025–4048. <https://doi.org/10.1002/jgrd.50355>
- Vicente-Serrano, S. M., Beguería, S., & López-Moreno, J. I. (2010). A multiscalar drought index sensitive to global warming: The standardized precipitation evapotranspiration index. *Journal of Climate*, 23(7), 1696–1718. <https://doi.org/10.1175/2009JCLI2909.1>
- Wang, Z., Guan, K., Sheffield, J., & Wood, E. F. (2016). Depiction of drought over sub-Saharan Africa using reanalyses precipitation data sets. *Journal of Geophysical Research: Atmospheres*, 121(18), 555–574. <https://doi.org/10.1002/2016JD024858>
- Willmott, C. J., & Matsuura, K. (1995). Smart interpolation of annually averaged air temperature in the United States. *Journal of Applied Meteorology and Climatology*, 34(12), 2577–2586. [https://doi.org/10.1175/1520-0450\(1995\)34<2577:SI>2.0.CO;2](https://doi.org/10.1175/1520-0450(1995)34<2577:SI>2.0.CO;2)
- Xie, P., Yatagai, A., Chen, M., Hayasaka, T., Fukushima, Y., Liu, C., & Yang, S. (2007). A gauge-based analysis of daily precipitation over East Asia. *Journal of Hydrometeorology*, 8(3), 607–626. <https://doi.org/10.1175/JHM583.1>
- Xu, L., Chen, N., & Zhang, X. (2019). Global drought trends under 1.5 and 2°C warming. *International Journal of Climatology*, 39(4), 2375–2385. <https://doi.org/10.1002/joc.5958>
- Yang, Y., Roderick, M. L., Zhang, S., McVicar, T. R., & Donohue, R. J. (2018). Hydrologic implications of vegetation response to elevated CO<sub>2</sub> in climate projections. *Nature Climate Change*, 9(1), 44–48. <https://doi.org/10.1038/s41558-018-0361-0>
- Yeh, S. W., Cai, W., Min, S. K., McPhaden, M. J., Dommenget, D., Dewitte, B., et al. (2018). ENSO atmospheric teleconnections and their response to greenhouse gas forcing. *Reviews of Geophysics*, 56(1), 185–206. <https://doi.org/10.1002/2017RG000568>
- Yuan, X., Wang, L., Wu, P., Ji, P., Sheffield, J., & Zhang, M. (2019). Anthropogenic shift towards higher risk of flash drought over China. *Nature Communications*, 10(1), 1–8. <https://doi.org/10.1038/s41467-019-12692-7>
- Yue, S., Pilon, P., Phinney, B., & Cavadias, G. (2002). The influence of autocorrelation on the ability to detect trend in hydrological series. *Hydrological Processes*, 16(9), 1807–1829. <https://doi.org/10.1002/hyp.1095>
- Zhang, J., Zheng, H., Xu, M., Yin, Q., Zhao, S., Tian, W., & Yang, Z. (2021). Impacts of stratospheric polar vortex changes on wintertime precipitation over the northern hemisphere. *Climate Dynamics*, 1–17. <https://doi.org/10.1007/s00382-021-06088-x>
- Zhang, W., Li, S., Jin, F. F., Xie, R., Liu, C., Stuecker, M. F., & Xue, A. (2019). ENSO regime changes responsible for decadal phase relationship variations between ENSO sea surface temperature and warm water volume. *Geophysical Research Letters*, 46(13), 7546–7553. <https://doi.org/10.1029/2019GL082943>